On the erosion of cohesive granular soils by a submerged jet: a numerical approach

Zeyd Benseghier, Li-Hua Luu, Pablo Cuéllar, Stéphane Bonelli, Pierre Philippe

Noname manuscript No.
(will be inserted by the editor)

On the erosion of cohesive granular soils by a submerged jet. A numerical approach

Zeyd Benseghier · Li-Hua Luu · Pablo Cuéllar · Stéphane Bonelli · Pierre Philippe.

Received: date / Accepted: date

Abstract This paper presents an erosion interpretation of cohesive granular materials stressed by an impinging jet based on the results of a micromechanical simulation model. The numerical techniques are briefly described, relying on a two-dimensional Lattice Boltzmann Method coupled with a Discrete Element Methods including a simple model of solid intergranular cohesion. These are then used to perform a parametric study of a planar jet in the laminar regime impinging the surface of granular samples with different degrees of cohesive strength. The results show the pertinence of using a generalized form of the Shields criterion for the quantification of the erosion threshold, which is valid for cohesionless samples, through empirical calibration, and also for cohesive ones. Furthermore, the scouring kinetics are analysed here from the perspective of a self-similar expansion of the eroded crater leading to the identification of a characteristic erosion time and the quantification of the classical erosion coefficient. However, the presented results also challenge the postulate of a local erosion law including erodibility parameters as intrinsic material properties. The paper then reviews the main limitations of the simulation and current interpretation models, and discusses the potential causes for the observed discrepancies, questioning the pertinence of using time-averaged macroscopic relations to correctly describe soil erosion. The paper concludes addressing this question with a complementary study of the presented simulations re-assessed at the particle-scale. The resulting local critical shear stress of single grains reveals a very wide dispersion of the data but nevertheless appears to confirm the general macroscopic trend derived for the cohesionless samples, while the introduction of cohesion implies a significant but systematic quantitative deviation between the microscopic and macroscopic estimates. Nevertheless, the micro data still shows consistently that the critical shear stress does actually vary approximately in linear proportion of the adhesive force.

Keywords Impinging jet · Laminar flow · Soil erosion · Granular cohesion · Lattice Boltzmann Method · Discrete Element Method.

Z. Benseghier
Associate researcher, PhD
Mines Saint-Etienne, Univ Lyon, CNRS, UMR 5307 LGF, 42023 Saint-Etienne, France
E-mail: zeyd.benseghier@emse.fr

L-H. Luu
Associate researcher, PhD
INRAE, Aix Marseille Univ, RECOVER, 3275 route de Cézanne, 13100 Aix-en-Provence, France.
E-mail: li-hua.luu@inrae.fr

P. Cuéllar
Research supervisor, PhD
BAM, Federal Institute for Materials Research and Testing, Division 7.2 for Buildings and Structures, Unter den Eichen 78, 12205 Berlin, Germany.
E-mail: pablo.cuellar@bam.de

S. Bonelli
Director of research, PhD
INRAE, Aix Marseille Univ, RECOVER, 3275 route de Cézanne, 13100 Aix-en-Provence, France.
E-mail: stephane.bonelli@inrae.fr

P. Philippe
Director of research, PhD
INRAE, Aix Marseille Univ, RECOVER, 3275 route de Cézanne, 13100 Aix-en-Provence, France.
E-mail: pierre.philippe@inrae.fr

1 Introduction

As a generic term, soil erosion refers to any situation where solid matter is progressively removed from a sediment bed under the mechanical action of an external agent such as a fluid flow or a solid body in motion. Many natural instances of soil erosion are commonly encountered in the context of

geological and geomorphological processes [38]. However, erosion can also pose serious risks to society by having an impact on the global carbon cycle [69] or being responsible for many catastrophic failures of civil infrastructures. In this sense, a particular concern in civil engineering is the risk associated to the hydraulic erosion of earthen structures [13, 14]. Specific estimations show that erosion is indeed the main cause for about 95% of the registered failure events in earthen hydraulic structures such as embankment dams, levees, and dikes [37, 61]. Erosional processes can take place at the external faces of a structure, as in the case of overtopping or overflowing events, but can also occur within the embankment or its foundation caused by water infiltration. The latter form is usually denoted *internal erosion* encompassing four distinct physical processes (namely, concentrated leak erosion, contact erosion, suffusion and backward erosion) [13, 14], whereby some of these involve at local scale the more usual configuration of soil erosion by a tangential water-flow.

It is therefore essential to be able to quantify the soil's resistance to erosion, which has led to the development of specific testing devices and procedures in the last decades. These require, in particular, the existence of a local law to be postulated, relating erosion rate and fluid flow strength at the exposed surface of the soil. The parameters introduced in such an erosion law are often called *erodibility* and conceptually considered as intrinsic properties of the soil. The Hole Erosion Test (HET) [8], the Erosion Functional Apparatus (EFA) [16] and the Jet Erosion Test (JET) [43] can be regarded as the devices most widely used for such assessment of the soil's resistance to erosion. The latter in particular has gained wide popularity due to its applicability to a broad range of soil types and its possible operation both in laboratory and field conditions, although it involves a far much complex flow configuration imposed by the immersed jet impingement. Relying on specific interpretation models for each test, the parameters of the erosion law can then be calibrated by adjustment to the experimental data obtained for a particular soil sample, leading this way to the assessment of the intrinsic soil's erodibility and to a possible classification in related charts.

In the absence of an appropriate theoretical background, erosion laws have so far been almost exclusively elaborated on an empirical basis [68], with no general consensus on the choice of the relevant quantities and on whether mean or distributed magnitudes of the relevant variables should be used, especially as regards the fluid flow action [34, 46, 52, 55]. A simple and commonly used law relies on a direct relation between the rate of erosion ϵ (i.e. volume loss by surface and time units) and the so-called excess shear stress that reads as the difference between the effective shear stress value τ exerted by the fluid flow at a given location of the soil's surface and a critical value denoted τ_c that accounts for soil's resistance against erosion [3, 46, 58]. In its most generic form, a power law relation can be used with introduction, in addition to τ_c, of two other parameters, namely an exponent n and a proportionality coefficient k_d called erosion coefficient. Alternatively, a dimensionless form can also be proposed by introducing the erosion rate coefficient $\epsilon_d = k_d \tau_c^n$. The excess shear stress law consequently reads:

$$\epsilon = \begin{cases} k_d(\tau - \tau_c)^n = \epsilon_d \left(\frac{\tau}{\tau_c} - 1\right)^n & if \quad \tau \geq \tau_c \\ 0 & if \quad \tau < \tau_c \end{cases} \tag{1}$$

In the related literature, the exponent n is commonly set equal to 1, particularly in the interpretation models for the HET [14] and JET [43] tests. However, when set free, n can be slightly higher or lower than unity but in any case it appears merely as a fitting parameter of experimental or numerical data which does not provide relevant physical significance [15]. On the contrary, both the critical shear stress τ_c and the erosion coefficient k_d (or alternatively the erosion rate coefficient ϵ_d) can be regarded as the so-called soil's erodibility, representing respectively the maximal resistance to fluid flow stress and the kinetics of soil's removal once erosion takes place.

Great effort has often been devoted to achieving a better understanding of these erodibility parameters, mainly by systematic confrontation and interlinking with some of the typical properties of natural soils. While a very large variety of empirical relations has emerged in the literature (partially listed e.g. in [14, 40, 71]), most of which are focused on the critical shear stress τ_c with little or no attention to the erosion rate parameter k_d, there is no broad consensus on the matter so far.

Concerning the critical shear stress τ_c, a straightforward extension of the classical cohesionless situation can be considered for some specific types of soils, namely those involving predominantly large grains but being however cohesive due to inter-particle bonds by a certain binding matrix. The resistance of non-cohesive sediments against fluid flow erosion is indeed known for about a century [19] through a given threshold value in terms of the dimensionless Shields number Sh_0 that compares superficial fluid shear stress τ to buoyant weight:

$$Sh_0 = \frac{\tau}{\Delta \rho g d} \tag{2}$$

The critical values of Sh_0 at erosion onset lie approximately along a general curve as a function of the shear Reynolds number Re_τ in the so-called Shields diagram. Note that Re_τ depends on τ through the shear velocity, complicating somewhat the use of this diagram [19]. One can more conveniently rely on several explicit empirical expressions provided in the literature [20, 34, 41] that relate the critical Shields number Sh_0^* to Re_τ^*, the shear Reynolds number at erosion onset.

When the soil grains are bonded, then the mechanical balance involves additional inter-particle adhesive forces, giving rise to a significant increase in the soil's resistance to erosion. In this case, the complexity of the related underlying mechanisms at the grain scale increases substantially, also including collective effects [71]. However, for moderately cohesive soils, cohesion can be simply added to the buoyant weight for a generalization of the Shields criterion [18, 23, 27, 49, 62, 67]. To this end, the introduction of a typical cohesive stress σ_{coh} is necessary, for instance as given by a macroscopic tensile strength, which can then be compared to the buoyant stress $\Delta\rho g d$ (with g the gravity, d the mean grain diameter, and $\Delta\rho$ the difference between grain density ρ_g and fluid density ρ_f) in the so-called dimensionless granular Bond number Bo_g [2, 21, 27] that reads:

$$Bo_g = \frac{\sigma_{coh}}{\Delta\rho g d} \tag{3}$$

Based on recent experimental results, Brunier-Coulin and co-workers proposed, with reasonable agreement, the following convenient form of generalized Shields criterion for moderately cohesive granular soils [18]:

$$Sh^* = \frac{\tau^*}{\Delta\rho g d + \alpha\sigma_{coh}} = \frac{{Sh_0}^*}{1 + \alpha Bo_g} \tag{4}$$

where τ^* stands for the critical fluid shear stress at the erosion onset. In this expression, Sh^* and Sh_0^* denote the critical values of the Shields number respectively in its generalized and traditional (i.e. cohesionless) forms for the corresponding critical shear Reynolds number Re_τ^*. It is straightforward to show that the cohesive Shields number Sh^* coincides with the usual definition Sh_0^* in the cohesionless case when Bo_g tends to zero, while it sharply decreases for high levels of cohesion, i.e. for $Bo_g \gg 1$. The coefficient α is presumably of order 1, arising from the dimensional analysis, through the two contributing resistant stresses (buoyant weight and cohesion). In this respect, Brunier-Coulin and co-workers found $\alpha_{3D} = 2.26 \pm 0.27$ from their experimental data carried out on millimetric glass beads bonded by solid resin bridges and eroded by an impinging jet in laminar regime [18].

The present study deals with the numerical simulation of these previous experiments, namely JET tests in a laminar flow condition impinging on cohesive granular samples. To this end, a relevant simulation method is required to account for both the hydrodynamics and the soil's behaviour during erosion. Only few works have focused on such simulation of soil's erosion by an impinging jet. A first option is to employ a pure CFD approach (Computational Fluid Dynamics), where the soil's surface is only considered as a boundary condition that evolves according to a prescribed erosion law [53, 54]. Alternatively, a mixed kind of modelling may also be performed both for 2D and 3D geometries, coupling a continuous description of the fluid flow (either by CFD or alternative methods) and a discrete description of the granular soil with the Discrete Element Method (DEM). This way, the interaction between fluid and grains can be properly included at small scale (grain-resolved simulation) and used to analyse erosion, either with purely cohesionless sands [11, 47] or bonded granular media [10, 29, 31]. Some notable contributions with the latter method have focused on the simulation of HET tests and discussed the relevance of both the excess shear stress law (Eq. 1 with $n = 1$) and an energetic approach [50, 66].

Our contribution here follows the same line of these latter studies involving bonded particles. It is based on a coupled approach with the Lattice Boltzmann Method (LBM) for the computation of the fluid dynamics in the porous space while the DEM scheme employed for the granular material includes a specific cohesion model governing the rheology and failure of the solid bonds [10, 36]. The resulting cohesive granular sample is fully saturated while the imposed flow conditions to induce erosion involve an impinging jet in the laminar regime, just as in the related experiments described in [18], but restricted here to a bi-dimensional geometry. Consequently, this study represents a direct extension to cohesive materials of the previous work by the authors dealing with the onset of impinging jet erosion for cohesionless granular samples [11]. A further novelty of this paper concerns the interpretation model and the inferred erodibility parameters. Finally, we also propose here a specific analysis of the crater dynamics to be compared to previous studies with cohesionless [26, 47] and weakly cemented sands [18].

The remainder of this paper is organized as follows. The numerical approach is first presented, including a brief description both of the methods employed for this study as well as of the jet configuration, parameters and research protocols adopted here. Then, we summarise the numerical counterpart of the usual interpretation procedure of impinging jet erosion, including the necessary adaptation of the model to the present 2D geometry and laminar flow conditions. Afterwards, the numerical results of the study are presented, focusing at first on the onset of erosion and on the derivation of a suitable dimensionless descriptor (a generalized form of the Shields number). We then address the resulting transient evolution of the scouring process and its related erosion law. Finally, we discuss the relevance and suitability of the current interpretation framework (i.e. the "inherent" soil erodibility parameters) in the light of our numerical results and review in a critical manner the specific assumptions and limitations of the presented model.

2 Numerical approach

2.1 Numerical methods

In essence, the present investigation at micro-scale relies on a combination of two classical numerical methods, namely

the Lattice Boltzmann Method (LBM) and the Discrete Element Method (DEM). The LBM permits the simulation of fluid flows through an explicit and discrete resolution of the Boltzmann equation. Following the Chapman-Enskog expansion [22], the incompressible Navier-Stokes can be recovered at small Mach numbers. The solid counterpart, i.e. the assembly of solid grains, is modelled here with the DEM, which accurately simulates multi-body interactions by frictional contacts and collisions. The present study is restricted to a 2D geometry, where the solid particles are represented by disks with a mean diameter d and a uniform grain size distribution in the range $[0.8d, 1.2d]$. A finer description of the two methods and of the way they are coupled is included here as supplemental data (see section "supplementary information"). The interested reader will find further details on our code and additional relevant references in [10, 11, 56].

Now let us specify two important quantities that will be used in the following, especially to evaluate the relevant dimensionless numbers. The first one is the microscopic adhesion force at contact, denoted F_c, adopted from the solid bond rheology proposed by Delenne and co-workers [33] to account for the presence of solid cohesive bridges at the intergranular contacts. This model includes three local degrees of freedom at contact (normal, tangential, rotation), associated with corresponding yield values for the pure normal, shear and bending interactions across the cohesive bond. For the mixed modes of de-cohesion, the model assumes a paraboloidal yield surface in the space of bond interactions based on experimental results with plane-strain granular samples. By adopting fixed relationships between the three yield values, the bond failure conditions are fully defined by a unique independent parameter, here the cohesion force F_c denoting the maximal pure tensile force before fracture. The second quantity of interest is the so-called "hydraulic" diameter $d_h = 0.8d$ of the solid particles that is used for the fluid flow calculation in the two-dimensional LBM-DEM coupling. This fictitious hydraulic diameter is actually the relevant size magnitude to be considered along with the hydraulic force acting on the particles.

2.2 Numerical set-up and parameters

2.2.1 2D impinging jet simulation

The flow configuration adopted for this study is a downward plane laminar jet originating from a nozzle of width b and impinging the horizontal surface of a cohesive granular sample (see Fig. 1).

The following LBM boundary conditions have been assumed for this study case: The solid walls forming the boundaries of the nozzle feature a bounce-back condition [24], while the exterior boundaries have all been implemented with a Zou/He outlet condition with zero pressure [72]. For the jet's nozzle of width b we impose a velocity inlet with a Poiseuille profile following the regularized method proposed in [48]. This way, the mean velocity of the Poiseuille jet flow at the nozzle reads $u_j = \frac{2}{3}u_0$, with u_0 being the maximal inlet velocity, and the corresponding jet Reynolds number is defined as $Re_j = u_j b/\nu$.

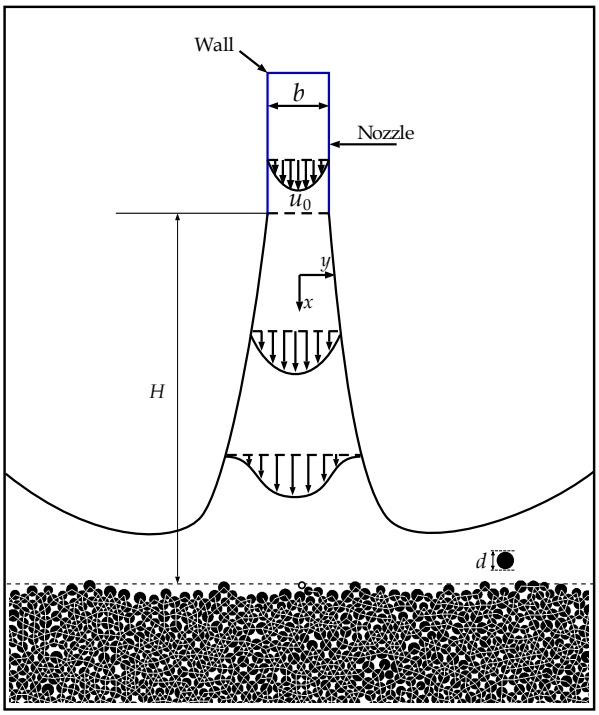

Fig. 1. Sketch of the impinging jet configuration considered in the present study.

2.2.2 Numerical procedures

Two different simulation protocols have been used in this study for the interpretation and quantification of the soil erodibility parameters. The first one aims at quantifying the critical shear stress at the onset of erosion while the second one addresses the time evolution of the scouring process.

Protocol A: Onset from increasing inlet velocity

The aim of this protocol is to determine the erosion threshold for a given cohesive granular sample. To this end, the maximal velocity of the jet inlet u_0 is progressively and linearly increased over time at a constant acceleration rate of 0.05 m/s^2. The simulation duration is fixed at 20 s. This way, we can identify the critical inlet velocity u_0^* based on the initiation of bonds breakage and the appearance of grain motion at the bed surface. This critical velocity can then be used to estimate the critical shear stress of the cohesive sample as explained hereafter.

We have repeated this procedure for different values of both the fluid kinetic viscosity ν and cohesion strength F_c (including the classical cohesionless case when $F_c = 0$),

as well as for three different granular samples with a mean diameter of d= 2, 3, and 5 mm, respectively. All three granular samples are generated polydisperse with a uniform grain size distribution, ranging from $d_{min} = 0.8d$ to $d_{max} = 1.2d$, and giving rise to very similar solid volume fractions around $\phi = 0.82 \pm 0.01$. The related data thus provide a large range of conditions to be displayed in the Shields diagram. The input parameters for this parametric study are summarized in Table 1.

Protocol B: Scouring with constant inlet velocity

Unlike the first protocol A, the jet inlet velocity is now maintained constant throughout the simulation of the jet erosion process. This protocol aims to investigate and quantify the scour kinetics based on an erosion law, consequently estimating the erodibility of the cohesive samples. In this respect, an adapted interpretation model is necessary for the 2D impinging jet erosion in a laminar regime (see Sec. 3) since the original JET interpretation model is only valid for a 3D flow configuration and turbulent jets.

In order to test the validity of our proposed interpretation model, we have performed a specific set of simulations with the parameters of series S2 (see Table 1) for different constant values of the maximal jet inlet velocity u_0, chosen in close proximity to the threshold velocity previously obtained with protocol A (namely for u_0 equal to 1.9, 2.0, and 2.2 m/s), while the cohesive bond strength F_c was varied systematically in the range of [1.0, 2.0] Newtons.

Table 1. Series used with the two protocols. In addition to the fluid density which is always $\rho_f = 1000$ kg/m^3, the other fluid's input parameters are the kinematic viscosity ν, the nozzle diameter b, and the impingement height H, while the particle diameter is d.

series	Protocol	d (mm)	ν (m^2/s)	b (mm)	H (mm)
S1	A	2	1×10^{-4}	6.6	70.1
S2	A, B	2	4×10^{-5}	5.0	70.0
S3	A	2	5×10^{-5}	6.6	70.1
S4	A	3	4×10^{-5}	6.7	70.4
S5	A	3	5×10^{-5}	6.7	70.4
S6	A	5	5×10^{-5}	6.0	70.1

2.3 Dimensionless numbers

According to the literature summarized in section 1, three relevant dimensionless numbers must be considered for the erosion of cohesive granular soils. Concerning the extension of the classical cohesionless situation, we first need to use the dimensionless numbers of the Shields diagram, namely the Shields number Sh_0 and the shear Reynolds number Re_τ, both calculated at the macroscopic scale from the maximal shear stress τ exerted by the flow at the top surface of the sample. Second, a proper definition of the granular Bond number Bo_g is then required to quantify the cohesion strength as defined, for instance, from a characteristic cohesive stress σ_{coh}, whose definition needs to be adapted to our 2D modeling conditions.

In our previous work on the subject, we proposed an expression for the maximal shear stress generated by the jet flow at the surface of a smooth horizontal wall in laminar flow conditions ($Re_j < 120$) and for a 2D geometry, and then proposed its extension to the case of a granular surface [11]. This relation, obtained by comparison to the classical free jet case and its related self-similar model, reads:

$$\tau^M = 0.137 \rho_f u_j^2 Re_j^{1/6} \left(\frac{H + \lambda}{b} \right)^{-2/3} \tag{5}$$

where H stands for the distance from the nozzle exit to the impingement surface while $\lambda = 0.036 Re_j b$ is the so-called virtual origin of the jet [11, 59]. The exponent M is used for "macroscopic" as the present empirical approximation is indeed obtained at the sample scale. For the two protocols used here, the jet Reynolds number reaches a maximal value only slightly larger than 200, a range where the expression in Eq. 5 is most probably still valid.

From this maximal macroscopic fluid shear stress τ^M, the standard definition for the shear velocity $u_\tau = \sqrt{\frac{\tau^M}{\rho_f}}$ holds but some adjustments are needed to account for the hydrodynamic forces on a grain in our 2D configuration. First, the hydraulic diameter $d_h = 0.8d$ must be used instead of the effective grain diameter d. Second, we propose to adapt the standard definition of the Shields number (Eq. 2) for a proper comparison to the experimental data and Shields curve by using a factor $\frac{8}{3\pi}$, accounting for the differences in cross section and volume between a sphere and a disk (see our previous study of the cohesionless case [11]). This way, we consider the following expressions for the classical Shields number and the shear Reynolds number in our 2D geometry:

$$\begin{aligned} Sh_0 &= \frac{8}{3\pi} \frac{\tau^M}{\Delta \rho g d_h} = \frac{10}{3\pi} \frac{\tau^M}{\Delta \rho g d} \\ Re_\tau &= \frac{u_\tau d_h}{\nu} = 0.8 \sqrt{\frac{\tau^M}{\rho_f}} \frac{d}{\nu} \end{aligned} \tag{6}$$

On this basis, we managed to compare successfully our numerical results with some previous experimental data for a plane jet impinging on cohesionless samples made out of glass beads provided by [5]. The resulting representation of the data in the classical Shields diagram was satisfactory, showing as well a reasonable agreement with the explicit formulation of the Shields curve, with nevertheless a slight overestimation [11]. It should additionally be noted that a qualitative agreement with experiments in axisymmetric geometry [17] has also been obtained.

Finally, as regards the additional contribution to resistant stresses induced by the solid bridges connecting the grains and denoted σ_{coh}, Brunier-Coulin and co-workers [18] suggested to use the macroscopic yield tensile stress τ_t, which they measured at sample scale. In their study, they also measured, when practicable, the maximal tension force F_t needed to break individually a given bond, and proposed an approximate relation between those quantities, $\tau_t \approx 1.25F_t/d^2$, as derived from Rumpf's equation [60] and assuming realistic values for the solid volume fraction and coordination number within their granular packings [4, 18]. By analogy, this proportionality relationship would read $\sigma_{coh} \approx F_t/d$ for the case of our 2D configuration. Here it is worth noting that this cohesion stress is expressed intendedly in units of N/m instead of Pa since we are dealing here with a 2D geometry. Regarding our cohesive bond model described in Sec. 2, we may simply identify F_t with the yield normal tensile force F_c, so that the 2D version of the granular Bond number to be used in the following eventually reads [36]:

$$Bo_g = \frac{\sigma_{coh}}{\Delta\rho g d} = \frac{F_c}{\Delta\rho g d^2} \tag{7}$$

Note that in this case the effective grain diameter d is considered here instead of the hydraulic diameter d_h since these forces pertain to the DEM part of the simulation model. Nevertheless, an alternative use of d_h would also lead to similar results solely changing the coefficient α in Eq. 4.

3 Analysing soil's erosion by an impinging jet

3.1 Original analytical model

In its basic version, the usual interpretation model of the Jet Erosion Test considers only the time evolution of the scouring crater depth right at the jet axis under the assumption that the erosion law in Eq. 1 holds, with $n = 1$ and with a rate of erosion expressed as $\epsilon = \frac{dx}{dt}$ (where x is the distance from the jet nozzle to the center of the crater) [43]. The final steady-state scour depth, which is approached asymptotically but not always easily measurable experimentally, was originally assumed to be given by an empirical relation [43]. However, recent studies in the literature have proposed several improvements and alternative methods either by employing different fitting procedures [32, 45, 51] or by considering the whole volume of eroded soil [42, 57, 63].

A questionable issue in this model concerns the expression considered for the characteristic fluid shear stress τ. This quantity is particularly difficult to measure, especially at a soil surface where a crater develops progressively, and generally can only be estimated based on strong hypotheses. Following previous studies on impinging jets over solid smooth walls [6, 7, 44], the expression $\tau = \frac{1}{2}\rho_f C_f V^2$ is commonly used, where V stands for the maximal vertical velocity at the same distance x from the nozzle as given by the self-similar model of a free jet [12, 65], and with the introduction of a friction coefficient C_f whose typical value is around 4×10^{-3} for turbulent flow conditions [1]. At this point it is worth noting that the JET interpretation model is based on a series of assumptions which are oversimplified and obviously unrealistic:

- The top of the soil sample is far from remaining flat and smooth during the test, while the stress model bears no consideration of the crater development.
- The maximal shear stress, even on a horizontal solid wall, is not located at the jet apex, where a stagnant point exists, but at some distance from the jet axis [7].
- The shear stress values along the soil surface where erosion occurs are widely distributed [7].
- The substantial impact of flow confinement is not considered [39].

Bearing in mind these reservations, which will be partly discussed afterwards, it is then possible to obtain a rather simple analytical expression for time as a function of scour depth and, after a proper fitting procedure, to deduce from the experimental data the two erodibility parameters of the tested soil specimen, even if a substantial dispersion can arise when using different fitting methods [32, 45, 51].

3.2 Adaptation to the present study

The previous JET interpretation model is not directly applicable to our particular situation for two main reasons: (i) the geometry here is that of a plane jet instead of the usual 3D axisymmetric jet; (ii) the flow regime remains laminar, far from the standard turbulent case. As detailed in the supplemental data of this paper (see section "supplementary information"), an adaptation of the model is proposed, based on the non-linear excess shear stress erosion law (Eq. 1) and on the appropriate expression for the maximal shear stress given by Eq. 5. This permits a straightforward derivation of two characteristics quantities, namely the critical shear-stress τ_c and the erosion time scale t_{er}, as follows:

$$\tau_c = \tau_\infty^M = 0.137\rho_f u_j^2 Re_j^{1/6} \left(\frac{x_\infty + \lambda}{b}\right)^{-2/3} \tag{8}$$

$$t_{er} = \frac{10.95b}{\rho_f u_j^2 Re_j^{1/6} k_d} \tag{9}$$

where x_∞ stands for the asymptotic distance from the nozzle to the crater floor (i.e. the maximal crater depth). The purely analytical resolution of the system is here no longer feasible and only a numerical resolution can be performed, which means that the exponent n must be prescribed and cannot be used as a free parameter. Nevertheless, we can reasonably

merge all cases where $n \neq 1$ simply by tuning the time scale with the empirical coefficient χ_n such that $t_{er_n} = \chi_n t_{er} = t_{er_{n=1}}$. A very good approximation for χ_n is given by $\ln(\chi_n) = 4.55(n-1)$.

Once this time-scale tuning adopted, we can limit ourselves to the case $n = 1$ for which one finds that all the scouring curves of Δx *versus* time obtained by exact numerical integration can be almost perfectly approximated by a standard exponential law (see section "supplementary information"):

$$\frac{\Delta x}{\Delta x_\infty} = 1 - \exp\left(-a\frac{t}{t_{er}}\right) \tag{10}$$

where a is a fitting parameter which depends solely on $\xi_0 = \left(\frac{H+\lambda}{b}\right)^{-2/3}$ and $\xi_\infty = \left(\frac{x_\infty+\lambda}{b}\right)^{-2/3}$.

For the sake of simplicity, this exponential approximation will be used in the forthcoming section to fit the numerical results. Interestingly, this trend is rather consistent with the crater depth evolution observed in purely granular soils scoured by a jet of impinging gas [26, 47].

4 Numerical results

4.1 Onset of jet erosion for cohesive samples

This section presents the results on the erosion threshold for a given cohesive strength of the granular sample when the inlet velocity is increased over time following protocol A as described in the previous section 2. Figure 2 shows a selection of snapshots for a typical simulation of the sample erosion. The full sequence for the whole simulation can be seen in the supplemental film video_S1 (See section "Supplementary Information").

The starting point of erosion can actually be well detected visually based simply on the inspection of a sequence of standard plots (here the particles' position and fluid velocities). In this example, the critical inlet velocity u_0^* for the onset of erosion is reached at time $t = 4.86$ s with an uncertainty below ± 0.03 s (i.e. the time difference between successive output frames), while the related absolute error on the critical velocity is thus $\pm 3.0 \times 10^{-3}$ m/s. In practice, the error bars are here smaller than the size of the symbol markers and are consequently not plotted in the following graphs. Alternatively, a criterion based on the total kinetic energy of the grains can also be employed to detect the onset of granular movement. Figure 3 shows the total kinetic energy of the sample *versus* time, which also yields an accurate measure of time at the erosion onset but without any significant improvement of its precision. Therefore, the visual criterion is consequently preferred for simplicity.

In any case, the kinetic energy of single particles can also be used to discriminate between eroded and non eroded grains. To this end, we have introduced a threshold energy value E_c, conveniently chosen somewhere in-between the typical kinetic energy levels observed at the very beginning of erosion, when only a few number of grains are in motion, and a minimal value arising from the intrinsic background noise of particle vibrations. As shown in Fig. 2, a critical threshold of $E_c = 2.0 \times 10^{-4}$ J permits to identify well the eroded state for particles with mean size $d = 2$ mm, depicted in white colour in the corresponding graphs.

The critical inlet velocities u_0^* observed at the erosion threshold for different bond strengths F_c, including the cohesionless case with $Fc = 0$, are shown in Figure 4, where a distinct correlation appears clearly. Furthermore, it is also apparent that a decrease in the mean particle size leads to an increase in the critical inlet velocity required to erode the particles for a given bond strength. In other words, here it becomes clear that for smaller particles the cohesive bond bears a stronger relative relevance, which makes them thus more difficult to be swept away. This is most probably due to the fact that the cohesion strength F_c is here assumed independent of the size of the bonded particles. In this respect, we envisage future works dealing with an appropriate definition of the bond yield conditions taking the particle-size into account and particularly relevant if broad grain size distributions are considered.

Next, the critical fluid shear stress τ_c^M and then the critical value of the classical cohesion-less Shields number Sh_0^* can be both estimated from the onset velocity $u_j^* = \frac{2}{3}u_0^*$ using Eq. 5 and Eq. 6, respectively. When plotted in the usual Shields diagram (Figure 5), the corresponding data of Sh_0^* increase monotonously with the critical shear Reynolds number Re_τ^* and, as F_c gets higher, they increasing depart from the Shields curve, which is provided here by the explicit formulation given in [41] that reads:

$$Sh_{Guo}^* = \frac{0.106}{Re_\tau^*} + 0.0545\left[1 - \exp\left(-0.158 {Re_\tau^*}^{0.52}\right)\right] \tag{11}$$

This result evidences that the classical Shields number definition, which is based solely on the buoyant weight and friction, is no longer appropriate when adhesive or cohesive forces are present at the grain scale. In practice, this is commonly observed for the case of fine sediments as rationalized for instance in [28].

Besides, when considering merely the values obtained without cohesion, we notice already a very substantial discrepancy between the measured data and the expected ones which should normally be close to the Shields curve approximated by Guo's law (Eq. 11). However, this deviation seems to be systematic and a fairly good agreement can thus be found by simply shifting the Shields curve *via* a multiplying coefficient denoted κ. As can be seen in Fig. 5, the best fit provides a value of $\kappa = 7.9 \pm 0.6$ (goodness of fit $R^2 = 0.754$). At present, we have no clear explanation for this marked over-

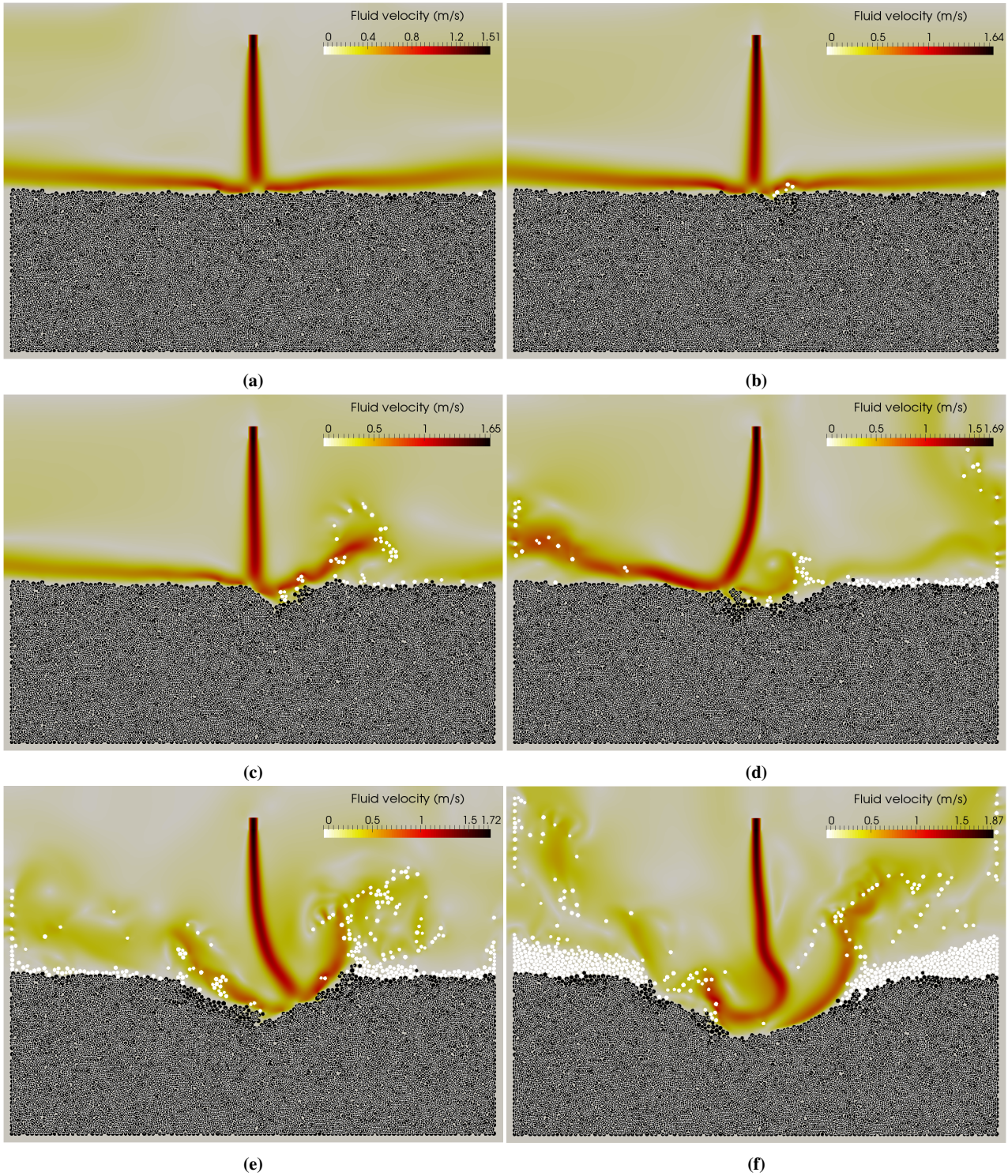

Fig. 2. Time sequence of a jet erosion on a cohesive granular sample, of cohesion strength $F_c = 1.2$ N, composed of 5,000 particles with $d = 2$ mm (series S2 of Table 1) for (a) $t = 2.56$ s, $Re_j = 126$, $u_0 = 1.51$ m/s; (b) $t = 4.86$ s, $Re_j = 136.5$, $u_0 = 1.64$ m/s; (c) $t = 5.12$ s, $Re_j = 137.7$, $u_0 = 1.65$ m/s; (d) $t = 5.89$ s, $Re_j = 141.2$, $u_0 = 1.69$ m/s; (e) $t = 6.4$ s, $Re_j = 143.6$, $u_0 = 1.72$ m/s; (f) $t = 8.96$ s, $Re_j = 155.4$, $u_0 = 1.87$ m/s. Solid particles with a kinetic energy above a critical threshold value $E_c = 2.0 \times 10^{-4}$ J are classified as eroded (here depicted in white colour). The cohesive bond network is displayed as white lines joining the centers of bonded particles.

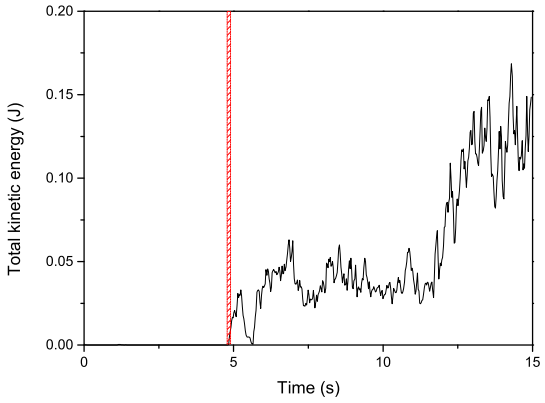

Fig. 3. Time evolution of the total kinetic energy of the grains during the jet erosion shown in Fig. 2.

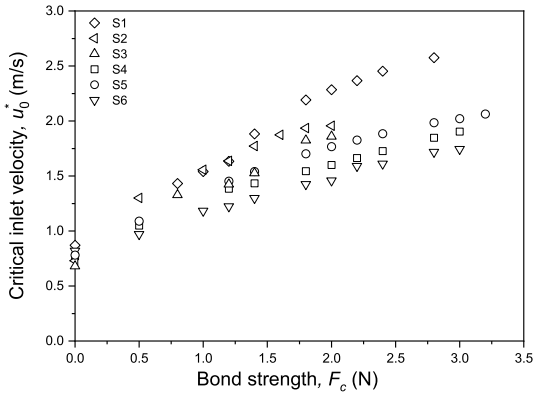

Fig. 4. Critical values of the inlet velocity u_0^* *versus* cohesive bond strength F_c for the simulated tests with different series from S1 to S6 (see Table 1).

estimation of the erosion threshold compared to the semi-empirical prediction of Shields. It should be noted, however, that our previous study had already highlighted this discrepancy, albeit to a lesser extent [11]. In the same vein, Choo and co-authors have shown that several parameters (packing density, particle shape, uniformity coefficient) could lead to an overestimation of the erosion threshold [25] but, again, clearly underneath a κ value around 8. In the end, the critical condition for cohesionless erosion that we will use in the following is empirically calibrated to $Sh^* = \kappa Sh^*_{Guo}$ without further physically sounded explanation regarding the rather high value obtained for κ.

In order now to test the generalization of the critical Shields number to cohesive granular soils as proposed by [18] and expressed in Eq. 4, it is first necessary to determine the optimal value of the dimensionless geometrical

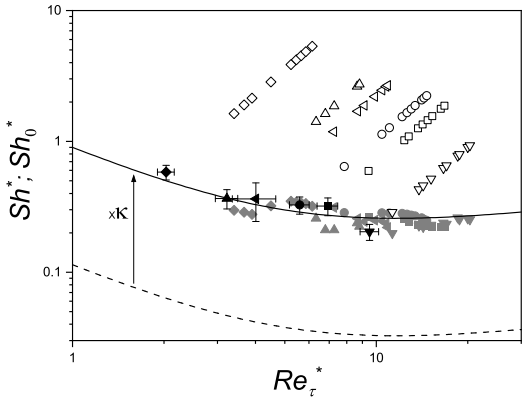

Fig. 5. Critical values of the usual Shields number Sh_0^* (open symbols, same as in Fig. 4) and of the generalized Shields number Sh^* (grey closed symbols) as functions of the critical shear Reynolds number Re_τ^*. The cohesionless data are also plotted (black solid symbols) and can be matched empirically to the theoretical Shields curve (dashed line given by Eq. 11), after simple multiplication by $\kappa = 7.9$ (solid line). The generalized Shields numbers Sh^* are calculated from Eq. 4 with $\alpha = 0.33$ and $\kappa = 7.9$.

coefficient α. To this end, and assuming that Sh^* lies on the empirically modified Shields curve, or equivalently that $Sh^* = \kappa Sh^*_{Guo}$, the following relation must be fulfilled according to Eq. 4:

$$\frac{Sh_0^*}{\kappa Sh^*_{Guo}} - 1 = \alpha Bo_g \tag{12}$$

Using our 2D definition for the granular Bond number given in Eq. 7, this relation is successfully tested in Figure 6 where a satisfactory agreement is found with the predicted proportional law. A linear regression with zero y-intercept gives $\alpha = 0.33 \pm 0.01$ (goodness of fit $R^2 = 0.976$). Note that this result is coherent with an expected value close to 1. Moreover, since $\kappa\alpha \approx 2.6$, it is also of the same order of magnitude than the corresponding experimental value of $\alpha_{3D} = 2.26 \pm 0.27$ found by [18], in 3D conditions and without cohesionless empirical calibration (i.e. for $\kappa = 1$).

Finally, a new plot of the values of Sh^* in Fig. 5 based on the same data and adopting $\alpha = 0.33$ in Eq. 12, gives a rather good agreement around the Shields curve and validates, through from the cohesionless empirical calibration, the suitability of the generalized Shields number to describe the erosion onset for cohesive granular samples instead of the classical Shields number. Moreover, this validation also somehow confirms and strengthens the previous findings by [18] based on experimental data. As a consequence, the generalized critical Shields number Sh^* can be used *a priori*

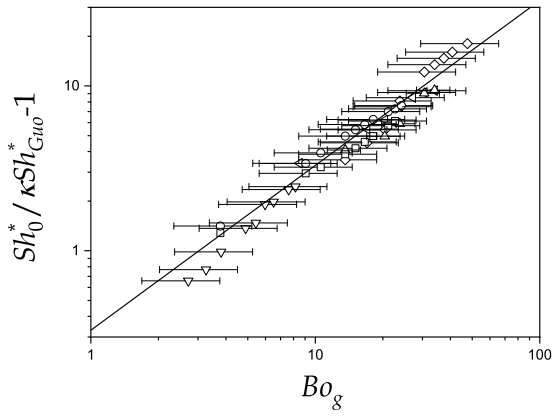

Fig. 6. Plot for all data of $\frac{Sh_0^*}{\kappa Sh_{Guo}^*} - 1$ *versus* the granular Bond number Bo_g, where Sh_0^* is the critical cohesionless Shields number obtained in the simulation, Sh_{Guo}^* is given by the implicit formulation of [41] in Eq. 11, and $\kappa = 7.9$. The symbols are the same as in Fig. 4 while the error bars arise from the width of the particle size distribution. The solid line represents a linear regression where the slope α is equal to 0.33 ± 0.01 with a correlation coefficient $R^2 = 0.976$.

as a reference value for predicting the macroscopic critical shear stress τ_c^M of our cohesive materials at the onset of erosion, which is supposed to coincide with the critical shear stress τ_c of the erosion law and whose presumed expression thus reads:

$$\tau_c = \tau_c^M = \Delta\rho g d Sh^* \left(1 + \alpha Bo_g\right) = Sh^* \left(\Delta\rho g d + \alpha \frac{F_c}{d}\right) \quad (13)$$

where the usual Shields number $Sh^* = \kappa Sh_{Guo}$ can be estimated from the explicit expression $Sh_{Guo}^*(Re_\tau^*)$ of [41] given by Eq. 11. In the present 2D geometry $\alpha = 0.33$, $\kappa = 7.9$, and Bo_g as defined in Eq. 7, while, in the more common 3D case, Brunier-Coulin and co-authors [18] found $\alpha = 2.26$, $\kappa = 1$, and Bo_g is given by Eq. 3.

Note additionally that this expression of the critical shear stress for surface erosion is somehow reminiscent to a closely similar linear relation between effective friction coefficient and granular Bond number found by Roy and co-workers when studying rheology of wet granular materials [64].

4.2 Scour kinetics and inferred erodibility

4.2.1 Time measurement of the crater depth

As exemplified by the red line in Figure 7, the shape of the crater can be obtained at any given time from basic image processing techniques with the help of the free software *ImageJ*. Two different methods were then tested to determine

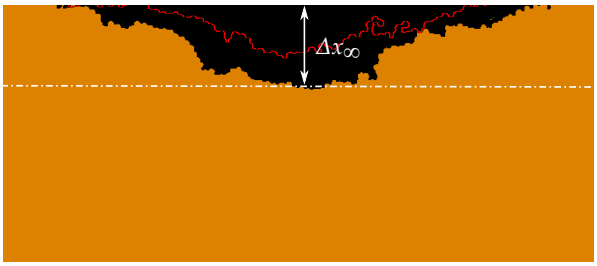

Fig. 7. A typical image resulted from post-processing techniques, using time average of the evolution of the scour area (black surface) once equilibrium is reached for $\Delta x_\infty = 23.5$ mm in series S2 with $F_c = 2$ N. The red line corresponds to the scour being excavated at $t = 1.0$ s while the final interface is obtained after averaging over the temporal range 3-8 s.

the crater depth Δx. The first one is based on a manual detection at each time step of the deepest position underneath jet impingement while the second assumes that the scour depth can be deduced from the crater area. This assumption is relevant in the context of a self-similar crater profile, with the width of the crater being proportional to its depth. Consequently, Δx is directly proportional to the square root of the surface A of the crater. The evolution of the scour depth thus reads:

$$\Delta x = \Delta x_\infty \left(\frac{A}{A_\infty}\right)^{1/2} \quad (14)$$

where A_∞ and Δx_∞ stand for the asymptotic values of the crater area and depth, respectively.

The scour area A can be measured automatically from the crater shape and reaches a steady-state after a while. The same holds for the crater depth Δx obtained from manually tracking the interface of the crater at its center. As shown in Figure 8, these methods (area and interface) give rather close results, especially at the equilibrium since they both reach approximately the same plateau Δx_∞: $\Delta x_\infty = 23.46$ mm and $\Delta x_\infty = 23.95$ mm for the area and the interface methods, respectively. As a consequence, both methods will give almost the same estimation of τ_c. However, the interface method generates more fluctuating data and a substantially slower kinetics, meaning that different values are expected for t_{er} and thereafter for k_d. This discrepancy at the beginning of the scouring process is probably due to the fact that the maximal shear stress along the soil surface, where erosion first starts, is not at the jet apex but located symmetrically at some distance. In addition to being simpler and automatic, the area method was preferred for being more integrative and less fluctuating.

In practice, the time evolution of the non-dimensional scour depth $\Delta x/\Delta x_\infty$ is obtained as follows. First, the evolution of A *versus* time allows to determine the temporal range where a steady-state is reached. Then, a time average

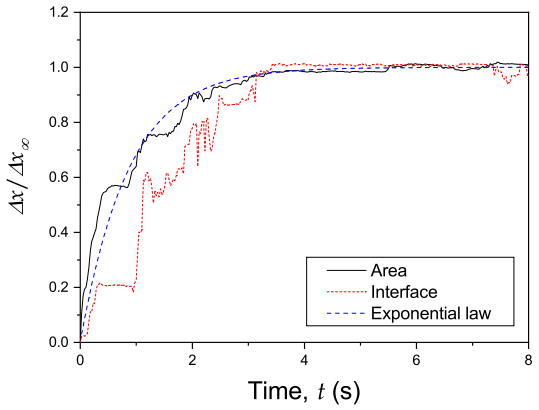

Fig. 8. Time evolution of the non-dimensional crater depth $\Delta x/\Delta x_\infty$ for the same parameters as in Fig. 7 (series S2 with F_c = 2 N) and with two different methods: Area (solid line in black) with Δx_∞ = 23.46 mm; Interface (dotted line in red) with Δx_∞ = 23.95 mm. The dashed solid line in blue stands for the following exponential law: $1 - \exp(-\omega t)$ with $\omega = 1.15$ s^{-1}.

over this range is performed to get precisely the shape of the steady crater. It is then possible to measure both the final depth Δx_∞ and the final area A_∞ and, finally, to calculate the crater depth Δx from Eq. 14.

4.2.2 Implementation of the new model

This section aims to test our 2D jet interpretation model, as developed in Sec. 3, and to quantify systematically the erodibility parameters. To do so, the series of simulations S2 (see Table 1) was conducted following protocol B. At the end of each simulation, image sequences obtained based on particle positions are saved, then a proper post-processing technique is performed to quantify the time evolution of the scour depth Δx from the crater area. Afterwards, the crater position $x(t) = x_0 + \Delta x(t)$ is calculated, especially its asymptotic value x_∞ reached at the equilibrium. This value is essential to determine the critical shear stress τ_c from Eq. 8.

From the typical evolution of the non-dimensional crater depth $\frac{\Delta x}{\Delta x_\infty}$ *versus* time t shown in Fig. 8, it is here once again apparent that a standard exponential law of the form $1 - \exp(-\omega t)$ can well account for the general trend. In this particular example, a coefficient $\omega = 1.15 \pm 0.02$ s^{-1} is obtained with a goodness of fit $R^2 = 0.948$.

As explained in the section dedicated to the interpretation model (see sec. 3), the exact solution of the scour depth evolution can be also approximated by an exponential function $1 - \exp\left(-a\frac{t}{t_{er}}\right)$ where a depends on ξ_0 and ξ_∞ (or equivalently on H, Re_j and x_∞). For instance, in the case presented in the supplemental data (see section "supplementary information") that corresponds to the post-processed data in Fig. 8, we found $a = (5.35 \pm 0.01) \times 10^{-3}$.

Finally, the adjustment of the numerical data with the model allows to identify the characteristic erosion time t_{er} as $t_{er} = a/\omega$. For the example shown in Fig. 8, one gets $t_{er} = a/\omega = (4.65 \pm 0.09) \times 10^{-3}$ s. Then k_d can be deduced from Eq. 9 and reads $k_d = (2.83 \pm 0.06) \times 10^{-3}$ m^3/N/s.

Based on a systematic use of this approach, Figure 9 presents the erodibility parameters k_d, ϵ_d, and τ_c deduced from our simulations for different values of the cohesive bond strength F_c, respectively.

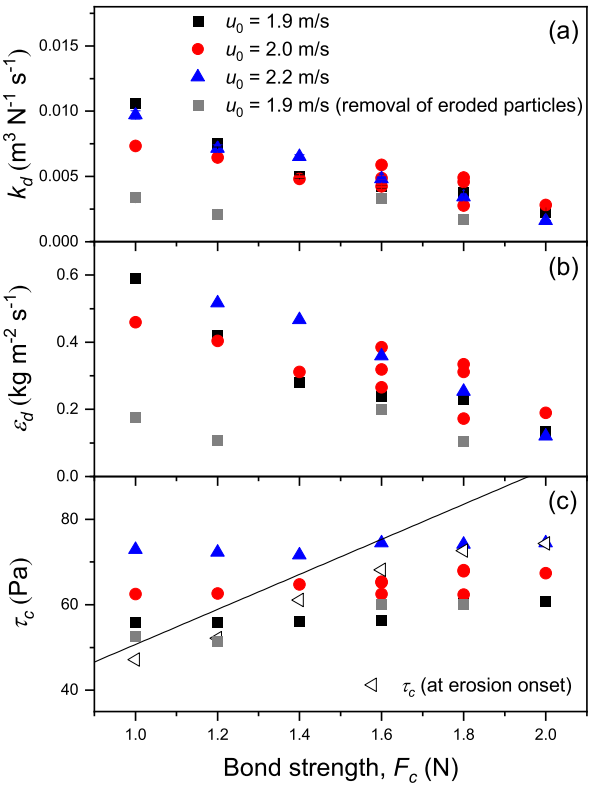

Fig. 9. Plot of (a) erosion coefficient k_d, (b) erosion rate coefficient, and (c) critical shear stress *versus* cohesive bond strength F_c obtained with three different inlet velocities: u_0 = 1.9 m/s (black square symbols), u_0 = 2.0 m/s (red circle symbols), and u_0 = 2.2 m/s (blue triangle symbols). An alternative method where the eroded particles are removed is also presented for u_0 = 1.9 m/s (grey square symbols). In graph (c), the data obtained for erosion onset in the previous section have been added (open symbols) while the solid line stands for Eq. 13.

As regards k_d and ϵ_d, two important points can be observed. First, both quantities consistently decrease when the cohesion strength gets higher. Second, for a given cohesion strength, the results vary moderately when the jet inlet velocity u_0 is changed, which is not expected since the erodibility parameters are supposed to be intrinsic of the material and should not depend on the fluid solicitation for any given cohesion strength. Note also that the variability induced by u_0 is somehow higher for ϵ_d than for k_d.

This unexpected dependency on u_0 also appears to hold for τ_c, but even in a far more pronounced manner, with an increase of up to almost 25 % when u_0 varies from 1.9 m/s to 2.2 m/s. In addition, for a given value of u_0, τ_c is only poorly dependent on F_c, whereas an almost linear relation would be expected both from Eq. 13 and from the values of the erosion onset τ_c^M obtained in the previous section. A substantial increase of τ_c with cohesion was also found from previous numerical HET tests [66].

5 Limitations of the current approach

5.1 A rather limited domain for cohesive surface erosion

In order to explore the range of applicability of the present approach, we performed a simulation for a slightly higher cohesive bond strength $F_c = 3.0$ N compared to the previous values studied in section 4. However, a new mode of degradation other than surface erosion was first observed in this case: although this soil is only marginally more resistant, a higher jet velocity (greater than 3 m/s) is required here for the onset of debonding, which leads to the appearance and quasi-instantaneous development of cracks throughout the sample, well before the first grain movements on the surface. Figure 10 shows this typical deep fracturing damage in the bond network, where the normal force between the particles that remain bonded is represented by positive (compressive) and negative (tensile) force values. As depicted here, two large cracks run through the entire depth of the sample. An erosion process then starts from the right-hand corner, which suggests a strong dependence on the boundary conditions.

In a previous numerical study, Benseghier [9] also observed such a crack opening that inhibited the surface erosion of a cemented granular material in a Couette shear flow configuration. To counteract this behavior, he proposed in the latter work to include a damage model [11], which enriches the DEM cohesion model with a time-dependency. Although interesting, this mode of degradation is outside the scope of the current paper. We can therefore conclude that the regime of damage and mass loss induced exclusively by surface erosion is only observed for very weakly cemented soils within a rather restricted range which, for series S2, almost corresponds to the extent of the parametric study conducted in Section 4: namely, the cohesive bond force F_c must be kept smaller than 2 N so that the jet velocity and the resulting maximal shear stress at the sample surface do not exceed apparent limit values of 2 m/s and 75 Pa, respectively.

5.2 Limitations of the macro-scale interpretation model

The results obtained from our interpretation model appear to question the general pertinence of the erodibility parameters, at least within the present methodological framework, since:

(i.) a variation of these parameters is observed for different jet inlet velocity u_0 but with a same cohesion strength F_c, and

(ii.) the critical shear stress τ_c as deduced from the model deviates significantly from the direct estimations obtained at the erosion onset.

In this respect, similar concerns have already been put forward by other experimental studies using different interpretation models for the Jet Erosion Test. In particular, the results presented by Khanal and co-workers [45] not only evidenced a similar variability of the erosion parameters with the jet injection velocity, initial nozzle to soil distance, and time intervals between two successive measurements, but also showed a large dispersion of data when using three different interpretation models.

In this study, it is clear that our new model for 2D laminar jet erosion is based on several assumptions whose validity can be questioned, as mentioned previously in section 3.1. Moreover, some peculiarities of our numerical system presented hereafter are responsible for a few specific issues that are improper of realistic erosion situations. The potential shortcomings of our approach are thus discussed and partly explained in the following paragraphs.

First of all, an intrinsic discrepancy between the presented model and the real scouring situations lies in our limitation to 2D geometries and laminar flow regimes. For this reason, and as already discussed more in depth in [11], the applicability of the present study remains limited and only qualitative comparisons can be obtained. Some differences between laminar and turbulent jets will also be discussed further below.

Another difference with respect to real situations in the field stems from the particular material considered here to represent the erodible soil, consisting in our case of relatively large grains effectively bonded by a solid bridge model. In practice, when such grains get debonded and eroded, they are far less likely to be carried away by the flow than for the case of a real soil made of considerably smaller particles. Consequently, most of the eroded grains remain trapped within the scour crater in our simulations. Such mobile layer of eroded particles created at the surface of the crater during scouring bears then a certain influence on our estimation of the scouring depth since it is considered as being part of the

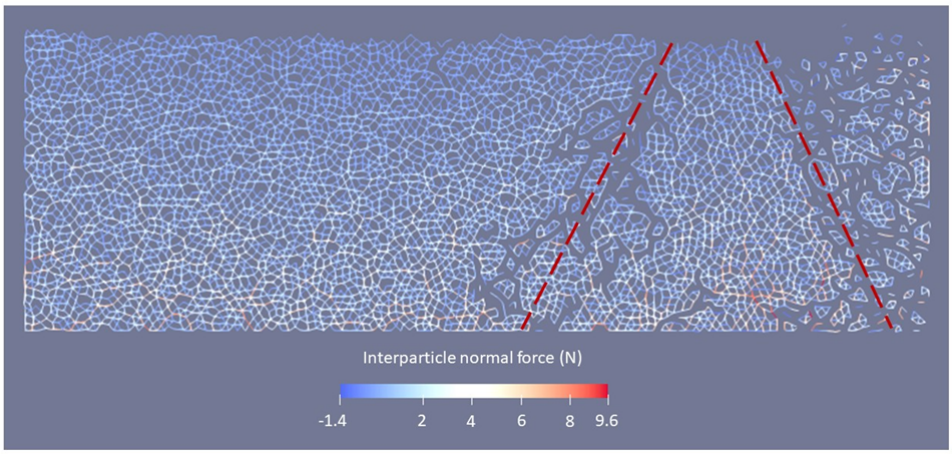

Fig. 10. Damaged granular sample of cohesive bond strength $F_c = 3.0$ N for series S2 (see Table 1): The unbroken bonds network displays two main oblique cracks through the sample height (red dashed lines).

remaining soil when the crater profile is obtained from image processing (see sec. 4.2.1). Moreover, this mobile granular layer can also play two distinct concurrent and counteracting physical roles during erosion: on the one hand, it can actually serve as a protective layer over the crater surface, shielding the subjacent grains from the erosive shear stresses imposed by the hydrodynamic flow. On the other hand, the eroded grains of this layer can also generate themselves further bond ruptures by granular collisions, specially for certain conditions of particle size and fluid flow (in general whenever the Stokes number of the entrained particles is greater than 1). The appearance of these numerical artifacts can nevertheless be counteracted in the simulation, for instance by specific removal of the eroded particles based on any suitable criterion (e.g. particles lacking cohesive bonds and with a kinetic energy above the critical value of $E_c = 2 \times 10^{-4}$ J as already introduced in sec. 4.1). In this respect, we have performed several complementary calculations to assess the effect of this systematic and arbitrary removal of all eroded grains for the particular study case of a jet velocity $u_0 = 1.9$ m/s. For comparison, the corresponding results are included with grey symbols in Fig. 9. Concerning τ_c, the discrepancy with the data obtained in the previous section at the erosion onset (protocol 1) is still significant although now a slight improvement is observed in the sense that the new data are somewhat closer to the expected linear evolution *versus* the cohesion strength F_c. More dispersion is found for k_d and, to a lesser extent, for ϵ_d, both quantities being now possibly compatible with a constant value whatever the value of F_c. Note that this still speculative outcome would be consistent with previous results by Sibille and co-workers based on numerical Hole Erosion Tests [66]. As detailed in sec 4.2.1, our scour depth measurement is based on the assumption that the crater remains self-similar during its development. This hypothesis appears somehow pertinent in view of the example presented in Fig. 7 and Fig. 8, which shows that the self-similarity assumption is acceptable except at the beginning of the scouring process. Any potential impacts of this assumption appear thus restricted to k_d and ϵ_d while τ_c would not be affected. In any case, here it is also worth noting that such a self-similarity has not been observed in more realistic conditions with 3D geometry and turbulent jet regime, see e.g. some recent experiments where systematic erosion profile measurements were performed during several JET tests [35, 57].

A much more questionable assumption concerns the use of the shear stress distribution over a flat wall to account for the fluid friction force inside the developing scour crater. This assumption, which clearly appears overly simplifying, is nevertheless common to all JET models as already mentioned in sec. 3.1, whereas the shape of the impinged surface obviously plays a key role. To investigate the impact of a curved surface, we therefore performed some additional LBM simulations of a 2D laminar jet impinging a circular concave wall. The configuration employed in this case is illustrated in Figure 11: the distance from the jet to the flat portion of the wall is $H = 73$ mm while the depth and radius of the circular excavation are $\Delta H = 17$ mm and $R = 35$ mm, respectively. Note that $R \approx H/2$ and $\Delta H \approx R/2$. A video file of the corresponding simulation entitled video_S2 can be accessed in the section "supplemental materials".

Figure 12 shows the shear stress distribution obtained for this particular geometry at the beginning of impingement (case shown in Fig. 11a). By comparison, the steady distribution obtained on a flat wall at the distance $H + \Delta H$ from the jet injection is also presented in Fig. 12 (red dashed line).

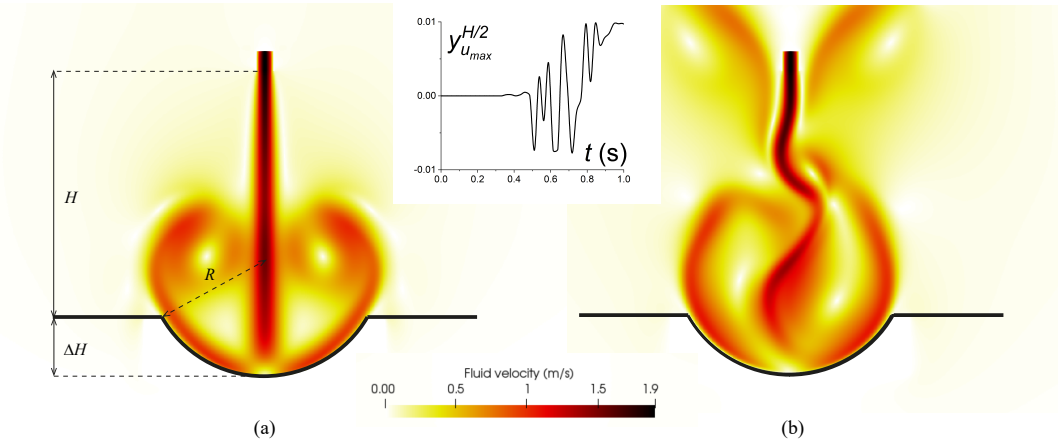

Fig. 11. Typical velocity magnitude field of a jet impinging on a concave surface (a) before and (b) after initiation of oscillations and flapping. The geometry as defined in sketch (a) is: $H = 73$ mm, $\Delta H = 17$ mm, and $R = 35$ mm. Inset: time evolution of the lateral position $y_{u_{max}}^{H/2}$ of the jet axis at a distance $H/2$ from the nozzle.

The stress distribution on the concave wall remains somewhat similar in shape with that of the flat wall but a substantial decrease in magnitude is observed, especially at the peaks which are actually used to quantify the characteristic shear stress [11]. Here, the relative decrease on the maximum shear stress is about 27 % as compared to the flat wall case that is used not only in our interpretation model but in all models proposed in the literature. Another critical difference observed with the concave impinged surface concerns the appearance of strong lateral oscillations of the jet as illustrated in Fig. 11. In fact, after impacting the circular excavation, the jet flow is deviated and re-directed towards the upper part of the plane jet just below the nozzle. Consequently, after a very brief initial moment, the jet is markedly disturbed by the upcoming reflected flow, giving rise to the strong oscillations of the jet flow evidenced in the inset of Fig. 11, where the lateral position $y_{u_{max}}^{H/2}$ of the jet axis (i.e. for $u = u_{max}$) at a distance $H/2$ from the nozzle is plotted *versus* time. This flapping can also be observed, but to a lesser extent, during the crater scouring of our cohesive-granular samples, as illustrated in Fig. 2. Therefore, the concurrence of these two effects due to the impingement on a crater, namely the shear stress reduction and the large jet oscillations, makes our interpretation model potentially unreliable, at least with respect to the quantification of the hydrodynamic stress generated by the flow during scouring. Similar complex hydrodynamic behaviours have been observed in the literature for turbulent gaseous or liquid jets on sandy beds, with some instances showing a loss of symmetry or quasi-periodic oscillations [26, 70].

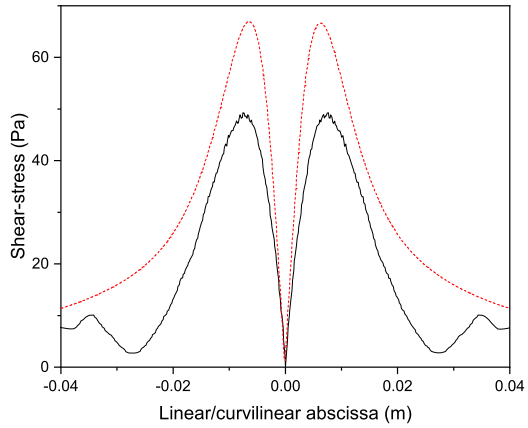

Fig. 12. Shear stress distributions in linear or curvilinear abscissa along the concave surface of Fig. 11 (black solid line) and along a standard flat surface at a distance $H + \Delta H$ from injection (red dashed line) with $b = 5$ mm, $u_0 = 1.9$ m/s and $\nu = 4 \times 10^{-5}$ m^2/s.

As another open question on the limitations of the present approach, one may also wonder, from a conceptual standpoint, about the legitimacy of comparing the critical shear stress as deduced from the interpretation model through the local erosion law with the one measured at the erosion onset. The former deals with a cessation of grain erosion while the latter accounts for the initiation of the process. The assumption that these two magnitudes should actually describe the very same unique threshold only appears to make sense in the absence of any hysteresis in the erosion mechanisms. To our knowledge, there is currently no evidence for this and we have not found any comprehensive study in the litera-

ture with, for instance, extensive cross comparisons between critical shear stress values deduced from an erosion law and direct measurements of erosion threshold generated by jet impingement that could answer this question appropriately.

Finally, and in a much more general way, one can rightfully question the relevance of using empirical time-average macroscopic relations to correctly describe soil erosion, a local phenomenon that occurs naturally at the level of the constituent grains of the material. This is notably the case for the description of local hydrodynamic quantities in the vicinity of the grains exposed to the flow, in particular the major simplification made by using the maximal value of the fluid stress obtained on a flat surface (see Eq. 5) as the actual value of the local shear-stress exerted on the soil sample surface. Indeed, this approximation, which we have already seen to be significantly flawed in a macroscopic vision due to the lack of consideration of the concavity of the eroded surface, is further challenged at the microscopic scale since it could turn out to be far from the reality at the grain level where important spatial and temporal fluctuations are expected to be observed. To address these questions, a complementary study is proposed hereafter by re-analysing the previous simulations on a particle scale basis, in line with some of our previous works [29, 30, 31].

6 Microscopic analysis

This analysis concerns the simulations of series S2 that provided the data in Fig. 4 to Fig. 9, limited to two cohesion strengths F_c = 1 N and F_c = 2 N, plus all the cohesionless configurations of the 6 series (S1 to S6) previously presented in Table 1.

6.1 Local quantities

We quantify here the action of the fluid flow on the individual grains both by the so-called hydraulic force, which is computed from a momentum balance when coupling the DEM and LBM models (see section "supplementary information"), and by a particle-scale shear stress. The latter corresponds to the maximal value of the viscous shear stress inside a square domain centered on a given particle i with a lateral magnitude of $d_i + 10dx$ (where d_i is the particle diameter and dx is the LBM lattice spacing). While these two hydrodynamic quantities, computable for each grain, do increase during the ramping sequence of the jet velocity, it can be noted that there is no obvious and systematic correlation between them as evidenced in Figure 13. We restrict the analysis here to the microscopic shear stress, denoted τ^m in the following (where the exponent m stands for "microscopic"), since, as a fluid shear stress, it advantageously allows direct comparisons with the previous macroscopic approach in terms of Shields number and shear Reynolds number.

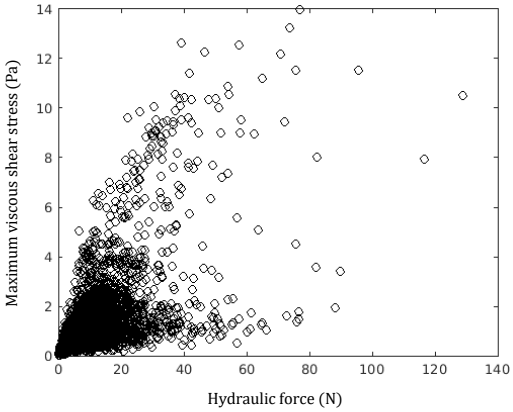

Fig. 13. Maximum viscous shear stress *versus* hydraulic force acquired for all grains at the surface prior to the erosion onset, for an impinging jet velocity going from 0.60 m/s to 0.63 m/s and without cohesion.

6.2 Individual erosion onset

Among all the kinematic quantities, the particle kinetic energy E_k^m appears as the best indicator of the initiation of grain movement. As shown in Figure 14a, an arbitrary threshold corresponding to 5% of the locally maximal value allows for a high precision in the detection of the first particle motion, both for cohesionless and cohesive samples (here series S2 with F_c = 1 N and F_c = 2 N). A typical particle erosion process is depicted in Figure14b, in the case where the adhesive force F_c = 2 N is large enough for the first particle detachment to consist of a pair of grains. Here, only the peak kinetic energy of the first eroded grain is used as reference energy for the entire erosion sequence since subsequent detached grains experience a much more complex kinematics due to possible interparticle collisions and ongoing adaptation of the local hydrodynamics as scouring develops. Note that the simulations were re-computed with a time step refinement in order to obtain a better accuracy on the erosion onset. In practice, the two time steps just before and just after the kinetic energy threshold are finely detected and allow the microscopic shear stress at onset τ_c^m to be calculated by linear interpolation.

6.3 Distribution of the critical local shear stress

By accumulating the values of τ_c^m for all eroded particles during each simulation of series S2 for F_c = 0, 1 and 2 N re-

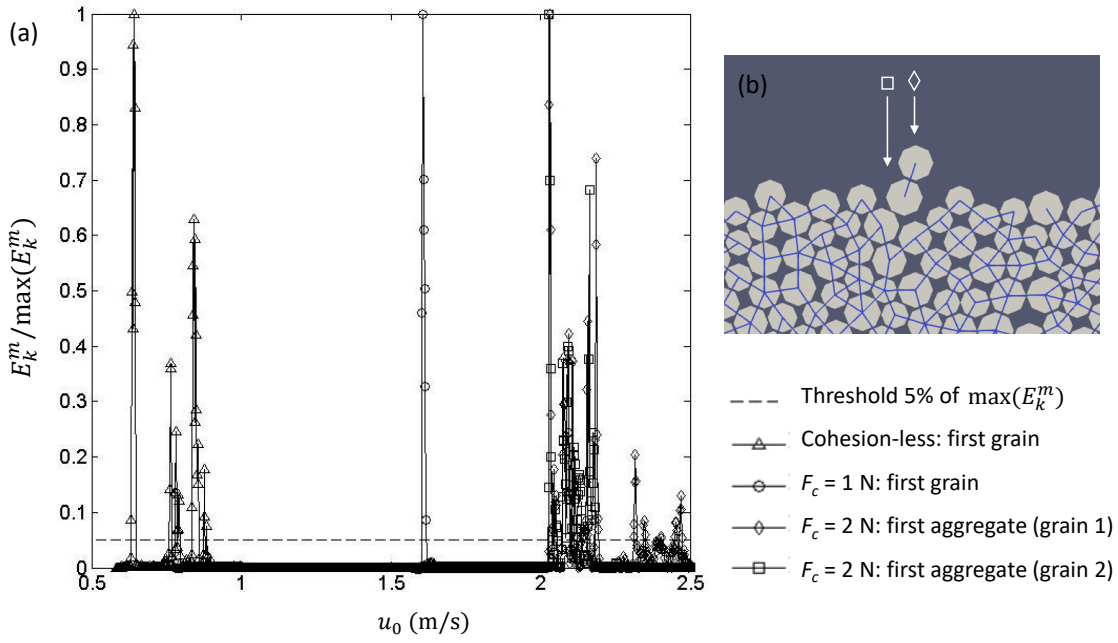

Fig. 14. Erosion onset determination: (a) First grains kinetic energy E_k^m normalized by its maximum as a function of the jet velocity u_0, for the cohesionless case, for $F_c = 1$ N and for $F_c = 2$ N. The dashed line stands for the threshold at $E_k^m/\max(E_k^m)$=5%. Note that, to save computation time, the increasing inlet velocity protocol does not start from 0 but from a well-chosen initial velocity. (b) Picture of the detachment of the first aggregate of two grains at the time step just after the threshold for the case $F_c = 2$ N (series S2).

spectively, the distributions obtained are shown in Figure 15. The first obvious finding is the huge spread of the distributions, which reveals a wide scattering of the resulting data, whether with or without cohesion. It should be noted that the values obtained with the very first eroded grains are not limited to a specific area of the distribution but are rather randomly located, as exemplified in Fig. 15 by the arrows and symbols corresponding to the early eroded particles shown in Fig. 14. This implies that the dispersion is intrinsic to the instantaneous erosion process and not due to a progressive drift of the distribution as the scour develops and the geometry changes. The local flow condition for erosion of a grain is therefore much more complex than a simple shear stress threshold given by the critical Shields number. Nevertheless, a mean value $\langle \tau_c^m \rangle$ with a substantial standard deviation can be derived from each distribution. A second observation that was expected is a shift in the distribution towards higher shear stress values with cohesion and a subsequent increase of $\langle \tau_c^m \rangle$ with F_c.

6.4 Macro/micro comparison and discussion

The values obtained in series S2 from both macro- and micro-scale analysis, namely τ_c^M and $\langle \tau_c^m \rangle$, can be compared in Figure 16 when plotted *versus* the granular Bond number Bo_g.

Without cohesion (i.e. when $Bo_g = 0$), the critical shear stress at micro-scale is found rather coherent with the one estimated by the previous macroscopic approach, around 11 Pa. We have repeated this microscopic analysis for the cohesionless case of each series, from S1 to S6, and a general consistency between micro and macro values is actually observed, with all the values ranging from 10 to 16 Pa, as can be seen in Table 2.

On the contrary, for cohesive samples, $\langle \tau_c^m \rangle$ is found substantially smaller in Fig. 16, almost by a factor 2, than the values of τ_c^M deduced from the empirical macroscopic shear-stress expression (Eq. 5), either directly at onset (empty symbols and dashed line for the corresponding linear regression) or from the general relationship proposed in Eq. 13 (solid line). A linear relationship seems however still to emerge

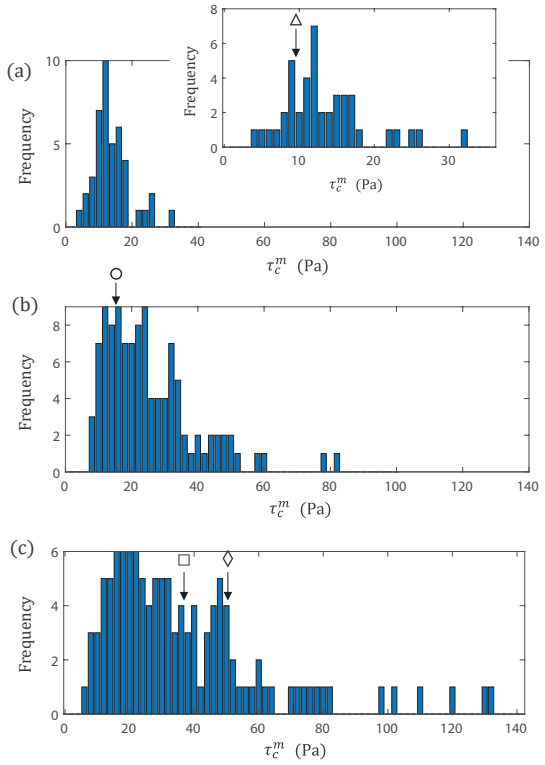

Fig. 15. Distributions of the local shear stress τ_c^m acquired at the interpolated kinetic energy threshold, for all eroded grains over the computation sequence, whereby the different panels correspond to: a) Cohesionless case (Inset: Same data using a finer scale in stress), b) F_c = 1 N, c) F_c = 2 N. The arrows and symbols indicate the critical values for the corresponding first eroded grains considered in Fig. 14.

Table 2. Mean critical shear stress without cohesion: τ_c^M from both macroscopic approach and $\langle\tau_c^m\rangle$ from micro-scale analysis. The error bars come either from the uncertainty on the first kinetic energy peak for τ_c^M or from the standard deviation of the distribution for $\langle\tau_c^m\rangle$.

series	τ_c^M (Pa)	$\langle\tau_c^m\rangle$ (Pa)
S1	16.1 ± 2.1	14.5 ± 3.9
S2	10.1 ± 3.3	13.3 ± 5.8
S3	10.2 ± 1.8	11.8 ± 7.5
S4	13.3 ± 2.1	10.9 ± 4.8
S5	13.6 ± 2.1	11.9 ± 5.3
S6	14.1 ± 2.0	12.8 ± 2.0

(see dotted line) but with caution given the huge error bars.

To conclude on this microscopic analysis, we can see that the comparison with the macroscopic approach is only compatible in the cohesionless case. This seems to confirm the observed overestimation of the Shields curve as evidenced

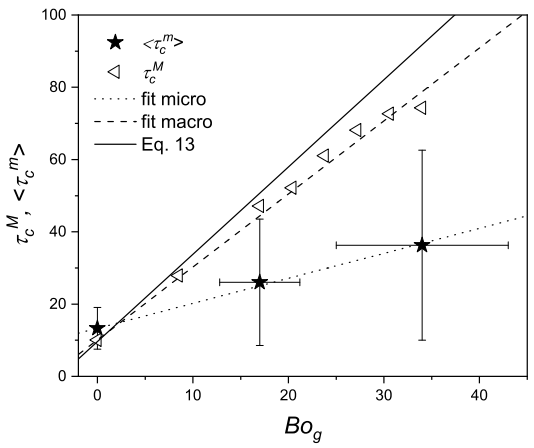

Fig. 16. Macroscopic and mean microscopic critical shear stress, respectively τ_c^M and $\langle\tau_c^m\rangle$, as a function of the granular Bond number Bo_g (series 2).

in Fig. 5 and consequently appears to support the necessary introduction of the previous empirical coefficient κ. In the cohesive case, the analysis reveals a large but systematic quantitative deviation between micro and macro values and shows, in a consistent manner, that the critical shear stress must increase approximately in proportion to the additional adhesive force F_c, or equivalently Bo_g. As a result there is no evidence to explain the very low dependence on F_c obtained for τ_c, the critical shear stress parameter of the erosion law, as deduced from the adapted interpretation model of the impinging jet erosion and shown in Fig. 9c.

7 Conclusions and outlook

The methods for the simulation of the impinging jet erosion on cohesive granular samples presented here and its macro-scale interpretation are capable of reproducing and quantifying the main physical mechanisms both at the erosion onset and throughout the crater scour, in fair comparison with previous data from similar experimental investigations.

In particular, the proposed generalized form of the Shields criterion for moderately cohesive soils including an appropriate definition of the cohesive Bond number makes it possible to collapse a wide range of our numerical results with varying particle sizes, flow conditions and cohesive strengths into a single universal trend that is well consistent with an explicit form of the classical Shields curve. In this respect, a systematic offset of the numerical data seems to call for the introduction of an empirical calibration factor in the threshold analysis.

Regarding the scouring kinetics, we show that the transient evolution of the crater depth can be well approximated

by an exponential function based on H, Re_j and x_∞, the latter being conveniently "measured" here assuming a self-similar expansion of the eroded crater. This allows the identification of a characteristic erosion time and the direct estimation of the classical erosion kinetics coefficient k_d.

However, the numerical results also highlight two important aspects, both of which call into question the appropriateness of the usual erodibility framework:

- For a given cohesion strength, the erodibility parameters depend significantly on the entry velocity of the jet, which undermines their assumption as intrinsic properties of the material.
- The critical shear stress derived at the final eroded steady-state deviates significantly from that estimated at the erosion onset

Several limitations of the numerical model and possible causes for the discrepancies with actual jet erosion have been discussed, all of which call for further examination and detailed study.

A first attempt to address these questions from a micromechanical perspective reflects the strong spatial and temporal fluctuations of the hydrodynamic fields at the grain scale, nevertheless also appearing to confirm the general macroscopic trend of critical shear stress derived for the cohesionless samples. Besides, the introduction of cohesion leads to a significant but systematic quantitative deviation between the microscopic and macroscopic estimates, whereby the micromechanical stress threshold still appears to consistently grow linearly with the cohesive strength.

In the perspective of future studies on the subject, we will aim to analyse simpler (and therefore better controlled) erosion configurations to test further the excess shear stress erosion law. This could be for example in the form of a direct shear erosion under steady Couette flow, which simplifies considerably both the geometry and the hydrodynamic conditions.

ACKNOWLEDGMENTS

Z. Benseghier is grateful for the financial support provided by the "Région Sud, Provence-Alpes-Côte d'Azur". The authors would also like to thank J.-Y. Delenne, F. Lominé, and J. Duriez for fruitful discussions. Centre de Calcul Intensif d'Aix-Marseille is acknowledged for granting access to its high performance computing resources.

Supplementary Information

Further details on the methodology including several additional explanatory figures (Fig. S1 to Fig. S5) along with the two referenced videos from the simulations (video_S1.mov and video_S2.mov) are available as supplementary materials.

References

1. Albertson, M.L., Dai, Y.B., Jensen, R.A., Rouse, H.: Diffusion of submerged jets. Trans. ASCE **115**, 639–697 (1950)
2. Anand, A., Curtis, J.S., Wassgren, C.R., Hancock, B.C., Ketterhagen, W.R.: Predicting discharge dynamics of wet cohesive particles from a rectangular hopper using the Discrete Element Method (DEM). Chem. Eng. Sci. **64**, 5268–5275 (2009). DOI 10.1016/j.ces.2009.09.001
3. Ariathurai, R., Arulanandan, K.: Erosion and deposition of cohesive soils. Journal of the Hydraulics Division **104**(2), 279–283 (1978). DOI 10.1061/JYCEAJ.0001165
4. Aste, T., Saadatfar, M., Senden, T.J.: Geometrical structure of disordered sphere packings. Phys. Rev. E **71**, 061302 (2005). DOI 10.1103/PhysRevE.71.061302
5. Badr, S., Gauthier, G., Gondret, P.: Erosion threshold of a liquid immersed granular bed by an impinging plane liquid jet. Physics of Fluids **26**(2), 023302 (2014). DOI 10.1063/1.4863989
6. Beltaos, S., Rajaratnam, N.: Impinging circular turbulent jets. Journal of the hydraulics division **100**(10), 1313–1328 (1974)
7. Beltaos, S., Rajaratnam, N.: Impingement of axisymmetric developing jets. Journal of Hydraulic Research **15**(4), 311–326 (1977). DOI 10.1080/00221687709499637
8. Benahmed, N., Bonelli, S.: Investigating concentrated leak erosion behaviour of cohesive soils by performing Hole Erosion Tests. European Journal of Environmental and Civil Engineering **16**(1), 43–58 (2012). DOI 10.1080/19648189.2012.667667
9. Benseghier, Z.: Numerical modeling of fluid flow erosion of a cohesive granular material. Ph.D. thesis (2019). URL `http://www.theses.fr/2019AIXM0579`. Engineering Sciences. Fluid mechanics and physics. Aix-Marseille University 2019
10. Benseghier, Z., Cuéllar, P., Luu, L.H., Bonelli, S., Philippe, P.: A parallel GPU-based computational framework for the micromechanical analysis of geotechnical and erosion problems. Computers and Geotechnics **120**, 103404 (2020). DOI https://doi.org/10.1016/j.compgeo.2019.103404
11. Benseghier, Z., Cuéllar, P., Luu, L.H., Delenne, J.Y., Bonelli, S., Philippe, P.: Relevance of free jet model for soil erosion by impinging jets. Journal of Hydraulic Engineering **146**(1), 04019047 (2020). DOI 10.1061/(ASCE)HY.1943-7900.0001652
12. Bickley, W.: The Plane Jet. The London, Edinburgh, and Dublin Philosophical Magazine and Journal of Science **23**, 727–731 (1937). DOI 10.1080/14786443708561847
13. Bonelli, S.: Erosion of geomaterials. Wiley-ISTE, New York (2012)
14. Bonelli, S.: Erosion in geomechanics applied to dams and levees. Wiley-ISTE, New York (2013)
15. Bonelli, S., Brivois, O.: The scaling law in the hole erosion test with a constant pressure drop. International Journal for Numerical and Analytical Methods in Geomechanics **32**(13), 1573–1595 (2008). DOI 10.1002/nag.683
16. Briaud, J.L., Ting, F.C., Chen, H.C., Cao, Y., Han, S.W., Kwak, K.W.: Erosion Function Apparatus for scour rate predictions. Journal of Geotechnical and Geoenvironmental Engineering **127**(2), 105–113 (2001). DOI 10.1061/(ASCE)1090-0241(2001)127:2(105)
17. Brunier-Coulin, F., Cuéllar, P., Philippe, P.: Erosion onset of a cohesionless granular medium by an immersed impinging round jet. Phys. Rev. Fluids **2**, 034302 (2017). DOI 10.1103/PhysRevFluids.2.034302
18. Brunier-Coulin, F., Cuéllar, P., Philippe, P.: Generalized Shields criterion for weakly cohesive granular materials. Phys. Rev. Fluids **5**, 034308 (2020). DOI https://doi.org/10.1103/PhysRevFluids.5.034308
19. Buffington, J.M.: The Legend of A. F. Shields. Journal of Hydraulic Engineering **125**(4), 376–387 (1999). DOI 10.1061/(ASCE)0733-9429(1999)125:4(376)
20. Cao, Z., Pender, G., Meng, J.: Explicit formulation of the Shields diagram for incipient motion of sediment. Journal of Hydraulic Engineering **132**(10), 1097–1099 (2006). DOI 10.1061/(ASCE)0733-9429(2006)132:10(1097)
21. Castellanos, A.: The relationship between attractive interparticle forces and bulk behaviour in dry and uncharged fine powders. Advances in Physics **54**(4), 263–376 (2005). DOI 10.1080/17461390500402657
22. Chapman, S., Cowling, T.G.: The mathematical theory of non-uniform gases: An account of the kinetic theory of viscosity, thermal conduction and diffusion in gases. Cambridge university press (1970)
23. Chen, D., Wang, Y., Melville, B., Huang, H., Zhang, W.: Unified formula for critical shear stress for erosion of sand, mud, and sand-mud mixtures. Journal of Hydraulic Engineering **144**(8), 4018046 (2018). DOI 10.1061/(ASCE)HY.1943-7900.0001489
24. Chen, S., Martínez, D., Mei, R.: On boundary conditions in Lattice Boltzmann Methods. Physics of Fluids **8**(9), 2527–2536 (1996). DOI 10.1063/1.869035
25. Choo, H., Zhao, Q., Burns, S.E., Sturm, T.W., Hong, S.H.: Laboratory and theoretical evaluation of impact of packing density, particle shape, and uniformity coefficient on erodibility of coarse-grained soil particles. Earth Surface Processes and Landforms **45**(7), 1499–1509 (2020)
26. Clark, A.H., Behringer, R.P.: Jet-induced 2-D crater formation with horizontal symmetry breaking. Granular Matter **16**, 433–440 (2014)

27. Claudin, P., Andreotti, B.: A scaling law for aeolian dunes on Mars, Venus, Earth, and for subaqueous ripples. Earth and Planetary Science Letters **252**(1-2), 30–44 (2006). DOI 10.1016/j.epsl.2006.09.004
28. Coleman, S.E., Nikora, V.I.: A unifying framework for particle entrainment. Water Resources Research **44**(4), W04415 (2008). DOI 10.1029/2007WR006363
29. Cuéllar, P., Benseghier, Z., Luu, L.H., Bonelli, S., Delenne, J.Y., Radjaï, F., Philippe, P.: Numerical insight into the micromechanics of jet erosion of a cohesive granular material. EPJ Web Conf. **140**, 15017 (2017). DOI 10.1051/epjconf/201714015017
30. Cuellar, P., Luu, L.H., Philippe, P., Brunier-Coulin, F., Benahmed, N., Bonelli, S., Delenne, J.Y., Ngoma, J.: Micromechanical features of jet erosion - A numerical perspective. 8th. International Conference on Scour and Erosion (2016)
31. Cuéllar, P., Philippe, P., Bonelli, S., Benahmed, N., Brunier-Coulin, F., Ngoma, J., Delenne, J.Y., Radjai, F.: Micromechanical analysis of the surface erosion of a cohesive soil by means of a coupled LBM-DEM model. IV International Conference on Particle-based Methods (PARTICLES 2015) p. 1121 p. (2015)
32. Daly, E.R., Fox, G.A., Al-Madhhachi, A.T., Miller, R.B.: A scour depth approach for deriving erodibility parameters from Jet Erosion Tests. Transactions of the ASABE **56**(6), 1343–1351 (2013). DOI 10.13031/trans.56.10350
33. Delenne, J.Y., El Youssoufi, M.S., Cherblanc, F., Bénet, J.C.: Mechanical behaviour and failure of cohesive granular materials. International Journal for Numerical and Analytical Methods in Geomechanics **28**(15), 1577–1594 (2004). DOI 10.1002/nag.401
34. Dey, S.: Entrainment threshold of loose boundary streams. Experimental Methods in Hydraulic Research. Series: Geoplanet: Earth and Planetary Sciences **1**, 29–48 (2011). DOI 10.1007/978-3-642-17475-9_2
35. Dong, C., Yu, G., Zhang, H., Zhang, M.: Scouring by submerged steady water jet vertically impinging on a cohesive bed. Ocean Engineering **196**, 106781 (2020). DOI 10.1016/j.oceaneng.2019.106781
36. Fan, J., Luu, L.H., Noury, G., Philippe, P.: DEM–LBM numerical modeling of submerged cohesive granular discharges. Granular Matter **22**, 66 (2020)
37. Foster, M., Fell, R., Spannagle, M.: The statistics of embankment dam failures and accidents. Canadian Geotechnical Journal **37**(5), 1000–1024 (2000). DOI 10.1139/t00-030
38. Fournier, A.: Soil Erosion: Causes, Processes, and Effects. Environmental science, engineering and technology series. Nova Science Publishers (2011)
39. Ghaneeizad, S.M., Atkinson, J.F., Bennett, S.J.: Effect of flow confinement on the hydrodynamics of circular impinging jets: Implications for erosion assessment. Environmental Fluid Mechanics **15**(1), 1–25 (2015). DOI {10.1007/s10652-014-9354-3}
40. Grabowski, R.C., Droppo, I.G., Wharton, G.: Erodibility of cohesive sediment: The importance of sediment properties. Earth-Science Reviews **105**(3-4), 101–120 (2011). DOI 10.1016/j.earscirev.2011.01.008
41. Guo, J.: Discussion of "The Albert Shields Story" by Junke Guo. Journal of Hydraulic Engineering **123**(7), 666–666 (1997). DOI 10.1061/(ASCE)0733-9429(1997)123:7(666.x)
42. Haddadchi, A., Rose, C.W., Olley, J.M., Brooks, A.P., McMahon, J., Pietsch, T.: An alternative method for interpreting Jet Erosion Test (JET) data: Part 1. application. Earth Surf. Process. Landforms **43**, 743–754 (2018). DOI 10.1002/esp.4270
43. Hanson, G., Cook, K.: Apparatus, test procedures, and analytical methods to measure soil erodibility in situ. Applied engineering in agriculture **20**(4), 455 (2004)
44. Hanson, G.J., Robinson, K.M., Temple, D.M.: Pressure and stress distributions due to a submerged impinging jet. In: Hydraulic Engineering, pp. 525–530. ASCE (1990)
45. Khanal, A., Klavon, K.R., Fox, G.A., Daly, E.R.: Comparison of linear and nonlinear models for cohesive sediment detachment: Rill erosion, Hole Erosion Test, and streambank erosion studies. Journal of Hydraulic Engineering **142**(9) (2016). DOI 10.1061/(ASCE)HY.1943-7900.0001147
46. Knapen, A., Poesen, J., Govers, G., Gyssels, G., Nachtergaele, J.: Resistance of soils to concentrated flow erosion: A review. Earth-Science Reviews **80**(1-2), 75–109 (2007). DOI 10.1016/j.earscirev.2006.08.001
47. Kuang, S., LaMarche, C., Curtis, J., Yu, A.: Discrete particle simulation of jet-induced cratering of a granular bed. Powder Technology **239**, 319–336 (2013). DOI https://doi.org/10.1016/j.powtec.2013.02.017
48. Latt, J., Chopard, B., Malaspinas, O., Deville, M., Michler, A.: Straight velocity boundaries in the Lattice Boltzmann Method. Phys. Rev. E **77**, 056703 (2008). DOI 10.1103/PhysRevE.77.056703
49. Lick, W., Jin, L., Gailani, J.: Initiation of movement of quartz particles. Journal of Hydraulic Engineering **130**(8), 755–761 (2004). DOI 10.1061/(ASCE)0733-9429(2004)130:8(755)
50. Lominé, F., Scholtès, L., Sibille, L., Poullain, P.: Modeling of fluid-solid interaction in granular media with coupled Lattice Boltzmann/Discrete Element Methods: Application to piping erosion. International Journal for Numerical and Analytical Methods in Geomechanics **37**, 577–596 (2013). DOI 10.1002/nag.1109
51. Mahalder, B., Schwartz, J.S., Palomino, A.M., Zirkle, J.: Estimating erodibility parameters for streambanks

with cohesive soils using the mini Jet Test device: A comparison of field and computational methods. Water **10**, 304 (2018). DOI 10.3390/w10030304

52. Marot, D., Regazzoni, P.L., Wahl, T.: Energy-based method for providing soil surface erodibility rankings. Journal of Geotechnical and Geoenvironmental Engineering **137**(12), 1290–1293 (2011). DOI 10.1061/(ASCE)GT.1943-5606.0000538
53. Mercier, F., Bonelli, S., Pinettes, P., Golay, F., Anselmet, F., Philippe, P.: Comparison of computational fluid dynamic simulations with experimental Jet Erosion Tests results. Journal of Hydraulic Engineering **140**(5), 04014006 (2014). DOI 10.1061/(ASCE)HY.1943-7900.0000829
54. Mercier, F., Golay, F., Bonelli, S., Anselmet, F., Borghi, R., Philippe, P.: 2D axisymmetrical numerical modelling of the erosion of a cohesive soil by a submerged turbulent impinging jet. European Journal of Mechanics - B/Fluids **45**, 36–50 (2014). DOI https://doi.org/10.1016/j.euromechflu.2013.12.001
55. Nearing, M.A., Norton, L.D., Bulgakov, D.A., Larionov, G.A., West, L.T., , Dontsova, K.M.: Hydraulics and erosion in eroding rills. Water Resources Research **33**(4), 865–876 (1997)
56. Ngoma, J., Philippe, P., Bonelli, S., Radjaï, F., Delenne, J.Y.: Two-dimensional numerical simulation of chimney fluidization in a granular medium using a combination of Discrete Element and Lattice Boltzmann Methods. Phys. Rev. E **97**, 052902 (2018). DOI 10.1103/PhysRevE.97.052902
57. Nguyen, V.N., Courivaud, J.R., Pinettes, P., Souli, H., Fleureau, J.M.: Using an improved Jet-Erosion Test to study the influence of soil parameters on the erosion of a silty soil. Journal of Hydraulic Engineering **143**(8), 4017018 (2017). DOI 10.1061/(ASCE)HY.1943-7900.0001305
58. Partheniades, E.: Erosion and deposition of cohesive soils. Journal of the Hydraulics Division **91**(1), 105–139 (1965)
59. Phares, D.J., Smedley, G.T., Flagan, R.C.: The wall shear stress produced by the normal impingement of a jet on a flat surface. Journal of Fluid Mechanics **418**, 351–375 (2000). DOI 10.1017/S002211200000121X
60. Pierrat, P., Caram, H.S.: Tensile strength of wet granular materials. Powder Technology **91**(2), 83–93 (1997). DOI 10.1016/S0032-5910(96)03179-8
61. Richards, K.S., Reddy, K.R.: Critical appraisal of piping phenomena in earth dams. Bulletin of Engineering Geology and the Environment **66**(4), 381–402 (2007). DOI 10.1007/s10064-007-0095-0
62. Righetti, M., Lucarelli, C.: May the Shields theory be extended to cohesive and adhesive benthic sediments? Journal of Geophysical Research: Oceans **112**(5) (2007). DOI 10.1029/2006JC003669
63. Rose, C.W., Olley, J.M., Haddadchi, A., Brooks, A.P., McMahon, J.: An alternative method for interpreting Jet Erosion Test (JET) data: Part 1. Theory. Earth Surf. Process. Landforms **43**, 735–742 (2018). DOI 10.1002/esp.4269
64. Roy, S., Luding, S., Weinhart, T.: A general(ized) local rheology for wet granular materials. New Journal of Physics **19**(4), 043014 (2017). DOI 10.1088/1367-2630/aa6141
65. Schlichting, H.: Boundary Layer Theory, 4th edn. McGraw-Hill (1960)
66. Sibille, L., Lominé, F., Poullain, P., Sail, Y., Marot, D.: Internal erosion in granular media: direct numerical simulations and energy interpretation. Hydrological Processes **29**(9), 2149–2163 (2015). DOI https://doi.org/10.1002/hyp.10351
67. Ternat, F., Boyer, P., Anselmet, F., Amielh, M.: Erosion threshold of saturated natural cohesive sediments: Modeling and experiments. Water Resources Research **44**(11) (2008). DOI 10.1029/2007WR006537
68. Tolhurst, T.J., Black, K.S., Paterson, D.M.: Muddy sediment erosion: Insights from field studies. Journal of Hydraulic Engineering **135**(2), 73–87 (2009)
69. Van Oost, K., Quine, T.A., Govers, G., De Gryze, S., Six, J., Harden, J.W., Ritchie, J.C., McCarty, G.W., Heckrath, G., Kosmas, C., Giraldez, J.V., da Silva, J.R.M., Merckx, R.: The impact of agricultural soil erosion on the global carbon cycle. Science **318**(5850), 626–629 (2007). DOI 10.1126/science.1145724
70. Vessaire, J., Varas, G., Joubaud, S., Volk, R., Bourgoin, M., Vidal, V.: Stability of a liquid jet impinging on confined saturated sand. Phys. Rev. Lett. **214**, 224502 (2020). DOI 10.1103/PhysRevLett.124.224502
71. Winterwerp, J.C., Van Kesteren, W.G.M.: Introduction to the Physics of Cohesive Sediment Dynamics in the Marine Environment, vol. 56. Elsevier (2004)
72. Zou, Q., He, X.: On pressure and velocity boundary conditions for the Lattice Boltzmann BGK model. Physics of Fluids **9**(6), 1591–1598 (1997). DOI 10.1063/1.869307